EES Batteries

ROYAL SOCIETY OF CHEMISTRY

PAPER

View Article Online
View Journal | View Issue

Cite this: *EES Batteries*, 2025, **1**, 1314

Liquid electrolyte-assisted stabilization of the LLZO/Li interface for stable lithium metal batteries

Mohammad Nasir, [a,b] Jun Seo,[a] Seo In Jung [a] and Hee Jung Park *[a,b,c]

Received 6th February 2025,
Accepted 28th July 2025

DOI: 10.1039/d5eb00026b

rsc.li/EESBatteries

Garnet-based solid-state batteries offer high energy density and improved safety but face challenges such as poor interfacial compatibility and high resistance at the LLZO/Li interface due to their lithiophobic nature. To address these issues, we applied small amounts of carbonate and ether-based liquid electrolytes to wet the surfaces of $Li_{6.25}Ga_{0.25}La_3Zr_2O_{12}$ (LLZO) pellets, enhancing wettability and reducing interfacial resistance. Cubic phase LLZO with a dense microstructure demonstrated an excellent ionic conductivity of 1.53 mS cm^{-1} and a low activation energy of 0.268 eV, enabling efficient Li-ion transport. Symmetric cell studies revealed superior performance with ether-based electrolytes due to the formation of a Li_3N/LiF rich interphase, achieving a significantly lower interfacial resistance (~32 Ω cm^2) and a higher critical current density (0.6 mA cm^{-2}) compared to carbonate-based systems. Long-term cycling tests confirmed the stability of ether-based cells, maintaining over 1000 h of stable cycling at 0.1 mA cm^{-2}. Full cells with $LiFePO_4$ (LFP) cathodes demonstrated excellent compatibility, retaining 78.5% capacity after 100 cycles with 99.9% coulombic efficiency. These results underscore the potential of minimal liquid electrolyte usage as a scalable and cost effective strategy to optimize the LLZO/Li interface for hybrid solid-state batteries.

Broader context

The transition to sustainable energy demands advanced storage solutions like lithium metal solid-state batteries, which offer high energy density and improved safety but face challenges such as interfacial resistance and dendrite formation. Garnet-based solid electrolytes like LLZO show promise due to their high ionic conductivity and stability, yet their lithiophobic nature hinders lithium compatibility. While strategies such as metallic coatings and chemical treatments address interfacial issues, they often lack scalability. In response to these challenges, we explore the use of minimal liquid electrolytes to enhance the LLZO/Li interface wettability, reducing resistance, improving Li-ion transport, and suppressing dendrite growth. This scalable and cost effective approach aligns with broader advancements in material design and interfacial engineering, contributing to the development of safer, more efficient next generation solid-state batteries.

1. Introduction

Lithium metal batteries (LMBs) have garnered significant attention to meet the growing demand for efficient and sustainable energy storage systems as they offer high theoretical energy density.[1–3] However, due to the use of traditional liquid electrolytes, LMBs suffer from flammability, dendrite induced short circuits, and limited electrochemical stability[4–7] To overcome these limitations, solid-state electrolytes (SEs) have been widely investigated as they offer improved safety, increased energy density, and the ability to use lithium metal anodes.[8–12]

Garnet-based systems, such as LLZO, are among the most promising candidates for solid-state lithium batteries due to their superior thermal and chemical stability, high ionic conductivity, and wide electrochemical window.[13,14] Nevertheless, the practical implementation of LLZO faces significant challenges when paired with Li metal anodes. The lithiophobic nature of the surface of LLZO leads to poor wettability, resulting in high interfacial resistance and non-uniform Li deposition.[15] These interfacial issues not only affect the charge transfer efficiency but also lead to Li dendrite formation, thus reducing the cycling stability of the cells.[15–17] Hence, interface engineering should be carried out deeply to uncover the full potential of garnet-based SEs for solid-state batteries.

In the literature, various interface strategies to reduce the interfacial resistance (area specific resistance, ASR) and improve the compatibility of garnet-based solid electrolytes with Li metal anodes have been explored. Metallic coatings,

[a]*Department of Materials Science and Engineering, Dankook University, Cheonan, 31116, Republic of Korea. E-mail: parkjang@dankook.ac.kr*
[b]*Hydrogen Research Center, Dankook University, Cheonan, 31116, Republic of Korea*
[c]*Department of Materials Science and Engineering, University of Washington, Seattle, WA, USA*

such as Au, Al, and Si, have been widely applied to improve wetting at the interface, achieving ASR values as low as ~50–150 Ω cm^2.[18–20] These coatings enhance Li contact with the garnet surface and facilitate ionic transport across the interface. Similarly, Li-based interlayers, such as Li_3PO_4 and LiF, have been employed to further reduce interfacial resistance by promoting better ionic conductivity and suppressing interfacial reactions.[21,22] Chemical surface treatments have also been utilized to modify the surface energy of LLZO, improving wetting and ensuring a more uniform interface.[23,24] Polymeric interlayers, including polyethylene oxide (PEO) based films, have been explored as well, serving as intermediate layers that bridge the gap between the garnet electrolyte and lithium metal.[25,26] These polymeric films enhance adhesion and improve the mechanical compatibility of the interface, thereby addressing the contact issues between the two surfaces.

Despite the progress achieved with these strategies, significant challenges remain in addressing interfacial resistance and ensuring long term stability. Many approaches involve complex fabrication techniques or materials that are prone to degradation over extended cycling. Metallic coatings, for instance, often face reactivity issues with Li, compromising their stability. Although Li-based interlayers and polymeric films are initially effective, their limited compatibility with garnet surfaces and low ionic conductivity contribute to an increase in ASR over time. Chemical surface treatments, although beneficial for improving wetting, often lack reproducibility and can introduce impurities that degrade the overall performance. These persistent issues highlight the difficulty of achieving a robust and stable interface that balances low ASR with practical scalability and reliability.

In this study, we propose an alternative approach for utilizing minimal amounts of liquid electrolytes (LEs) such as carbonate and ether-based LEs to enhance the wettability and ionic conductivity at the LLZO/Li interface. Unlike complex deposition or treatment processes required for other strategies, the application of liquid electrolytes is straightforward, scalable, and cost effective. This study bridges the gap by examining the interfacial resistance and compatibility of LLZO with carbonate and ether-based LEs in symmetric cells, alongside its application in full cells with $LiFePO_4$ (LFP) cathodes. This approach reduces the physical gaps between the LLZO and Li, reducing interfacial resistance and ensuring uniform Li-ion transport, thereby suppressing dendrite growth and enhancing long term cycling stability. Ether-based electrolytes, in particular, demonstrate significant advantages over conventional approaches, achieving ASR values as low as ~32 Ω cm^2. These systems also exhibit a critical current density (CCD) of ~0.6 mA cm^{-2}, highlighting their ability to sustain high current densities without inducing dendrite formation, enabling stable long term cycling, maintaining over 1000 h of operation at 0.1 mA cm^{-2}, and delivering an excellent capacity retention of 78.5% after 100 cycles with a coulombic efficiency (CE) of 99.9% in full cells with LFP cathodes.

2. Experimental

Ga doped LLZO was synthesized *via* a solid state reaction method using stoichiometric amounts of Li_2CO_3 (Soekawa Chemicals, 99.9%), La_2O_3 (High Purity Chemicals, 99.9%), ZrO_2 (Samchun Chemicals, 99.9%), and Ga_2O_3 (High Purity Chemicals, 99.9%). The precursors were ball milled in isopropanol for 24 h, with 5 wt% excess Li_2CO_3 added to compensate for lithium loss during sintering. The mixture was calcined at 850 °C for 6 h, ground, and further milled to achieve finer particle sizes. The resulting powder was pressed into pellets at 200 MPa using a cold isostatic press and sintered in air at 1200 °C for 6 h. The sintered pellets were polished and prepared for structural and electrochemical testing.

The structural properties were analyzed using X-ray diffraction (XRD, Rigaku) with Cu K_α over the 2θ range of 10–70° and Raman spectroscopy (NANOBASE Inc.) with a 532 nm laser. Microstructural analysis was performed with a scanning electron microscope (Compact SEM Seron, AIS2000C). Li-ion conductivity was measured *via* electrochemical impedance spectroscopy (EIS) (Zurich Instruments MFIA) with a 20 mV AC signal over a frequency range of 1 Hz to 5 MHz and a temperature range of 5–65 °C. Symmetric Li|LLZO|Li cells were assembled in CR2032 type coin cells using minimal amounts of carbonate (1 M $LiPF_6$ in EC/EMC (1 : 2 v/v) with 5 wt% FEC) or ether-based (1 M LiTFSI in DOL/DME (1 : 1 v/v) with 2 wt% $LiNO_3$) LEs to ensure proper interfacial contact. The surface chemistry of the LLZO/Li interface was examined using X-ray photoelectron spectroscopy (XPS, Scientific K-Alpha system, Thermo Scientific). Galvanostatic cycling tests were performed using a battery cycler (Won-A-Tech) to evaluate the interfacial stability and long term performance at different current densities. Full Li|LLZO|LFP cells were fabricated with LFP cathodes prepared by coating a slurry of LFP, conductive carbon, and PVDF in an 8 : 1 : 1 weight ratio onto aluminum foil. Approximately 0.5 μL of ether-based LE was applied to improve interfacial contact on both sides of the LLZO pellets. The cells were heated at 60 °C for 24 h prior to testing and subsequently evaluated at the same temperature under a 0.1C charge/discharge rate.

3. Results and discussion

Fig. 1(a) shows the X-ray diffraction (XRD) pattern of Ga doped LLZO, compared with the standard diffraction pattern of cubic LLZO. The data confirm that LLZO crystallizes predominantly in the cubic garnet structure, as evidenced by the excellent agreement between the observed diffraction peaks and the standard cubic phase (PDF#97-026-1302). Key reflections such as (420), (332), and (422) are well defined, and no additional peaks corresponding to secondary phases, such as Ga_2O_3 or $La_2Zr_2O_7$, are detected. This indicates the successful incorporation of Ga into the garnet lattice without forming undesired byproducts. The sharp and symmetric diffraction peaks reflect the high crystallinity of the material, with no evi-

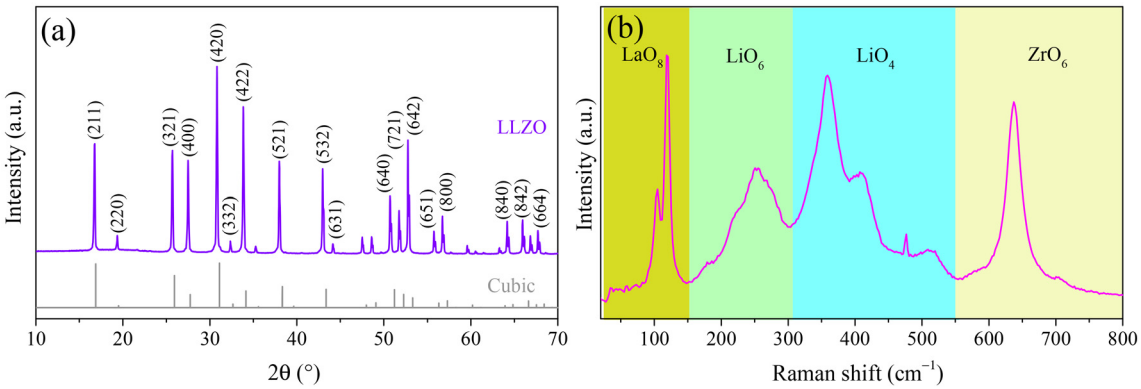

Fig. 1 (a) XRD pattern of LLZO with a standard cubic garnet phase confirming its cubic phase structure. (b) Raman spectrum further validating the cubic phase formation.

dence of peak splitting associated with the tetragonal phase. This confirms that Ga doping effectively stabilizes the cubic structure by influencing the local environment of the lattice.

Fig. 1(b) presents the Raman spectroscopy data, further validating the cubic garnet structure. The spectrum reveals characteristic vibrational modes of the cubic phase. Peaks in the low frequency region (<150 cm^{-1}) correspond to La–O stretching vibrations within the garnet framework, while those in the mid frequency range (150–550 cm^{-1}) are assigned to Li–O stretching and bending vibrations, confirming the occupation of Li in the LLZO lattice.[27] Notably, no peaks indicative of secondary phases, such as carbonate or hydroxide species, are observed, emphasizing the high purity of the sample. Additionally, the absence of peak splitting in the Raman spectrum supports the conclusion that Ga-doped LLZO adopts a pure cubic phase without any contribution from the tetragonal phase.[13,27] Thus, XRD and Raman spectroscopy confirm that Ga doping stabilizes the cubic LLZO structure and ensures the formation of a highly crystalline, phase pure material.

As shown in Fig. 2(a), SEM reveals a dense and uniform microstructure for LLZO sintered at 1200 °C, with closely packed grains and negligible porosity, indicative of effective sintering. Such a dense microstructure reduces grain boundary resistance and improves mechanical properties, which are crucial for enhancing ionic conductivity. The elemental maps shown in Fig. 2(b–e) demonstrate the uniform distribution of La, Zr, and O, confirming their effective incorporation into the LLZO structure. However, Ga exhibits partial segregation along the grain boundaries, as seen in Fig. 2(d). This behavior is commonly observed in Ga-doped LLZO and is attributed to liquid-phase-assisted sintering, where Ga promotes grain growth and enhances overall densification.[28,29] The EDS spectrum in Fig. 2(f) further supports the presence of all constituent elements with distinct peaks corresponding to their characteristic energies. The relative atomic ratios of elements confirm the compositional integrity and phase purity of the synthesized material.

Temperature dependent EIS was employed to gain insights into the electrochemical behavior of LLZO. Fig. 3(a) presents

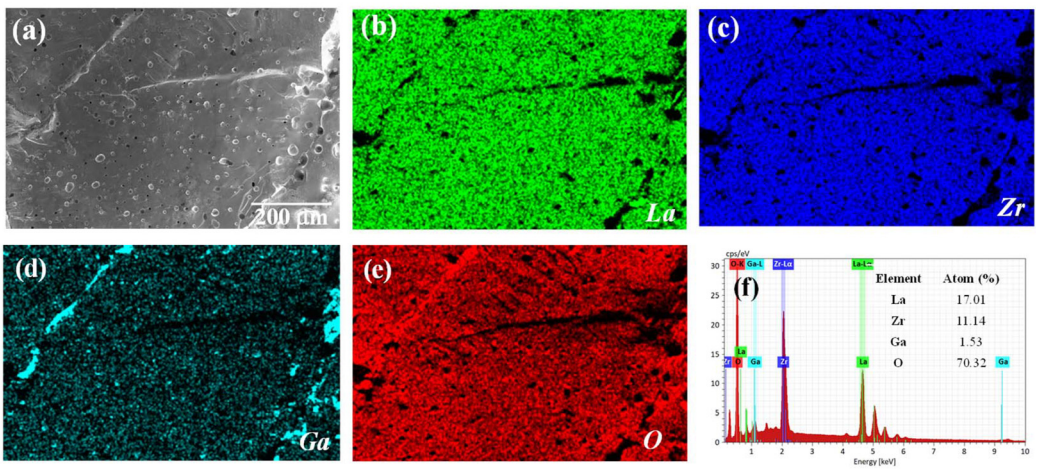

Fig. 2 Microstructural and compositional properties of LLZO: (a) SEM image, (b–e) 2D maps of the constituent elements, and (f) EDS spectrum showing the presence of La, Zr, Ga, and O.

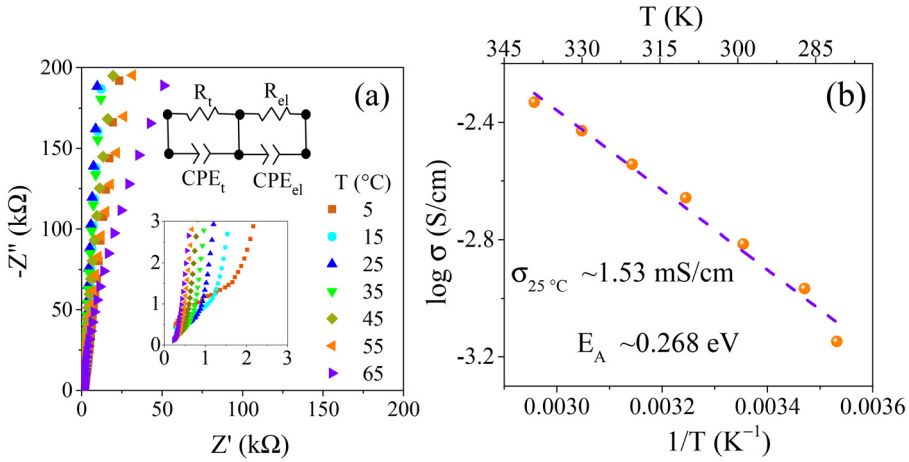

Fig. 3 (a) Nyquist plots of impedance spectra measured at various temperatures, with a zoomed-out view and an equivalent circuit model shown in the insets. (b) Arrhenius plot of temperature dependent ionic conductivity, indicating low activation energy.

the impedance behavior of LLZO at different temperatures, along with the equivalent circuit model used for fitting the data. The Nyquist plot exhibits typical semi-circular arcs at higher frequencies, corresponding to the bulk (R_b) and grain boundary resistance (R_g), followed by a tail at lower frequencies associated with electrode polarization (R_{el}). The inset provides a zoomed-out view of the high frequency region, showing a highly depressed semicircle, which indicates indistinguishable contributions from bulk and grain boundary resistances. Therefore, the data were simulated using an equivalent circuit model consisting of two parallel RC circuits composed of R_t (total resistance of the pellet) and R_{el} resistances, and CPE_t and CPE_{el} constant phase elements.[30] A good match was achieved between the experimental and simulated impedance patterns based on equivalent circuits, revealing a reduction in impedance with increasing temperature.

Fig. 3(b) shows the temperature dependence of the ionic conductivity (total) of LLZO. The conductivity was estimated from the following relation using the dimensions of the pellet.

$$\sigma_{total}(T) = \sigma_0 e^{(-E_A/k_B T)} \quad (1)$$

where σ_0 is a pre-exponential factor and T is the absolute temperature. E_A and k_B denote the activation energy and Boltzmann constant, respectively. The data show a linear relationship between $\log \sigma$ and $1/T$, indicating thermally activated ionic transport governed by the Arrhenius equation. The calculated room temperature ionic conductivity is approximately 1.53 mS cm^{-1}, which competes with the high values of conductivity reported for garnet-based solid electrolytes.[14,31–34] The observed low activation energy of 0.268 eV confirms an excellent mobility and thus efficient Li-ion transport through the cubic LLZO.

EIS and cycling tests were conducted to systematically assess the impact of different LEs on the electrochemical performance of Li|LLZO|Li symmetric cells fabricated with LLZO as a SE (Fig. 4). As shown in Fig. 4a, the Nyquist plots reveal substantial differences depending on the LE used. To quantify the interfacial resistance, the impedance spectra were fitted using an equivalent circuit model comprising two parallel RC elements: R_{SE} and CPE_{SE}, representing the bulk and grain boundary resistance/capacitance of LLZO, and R_{int} and CPE_{int}, representing the interfacial resistance and non-ideal capacitance at the LLZO/Li interface (inset, Fig. 4a).[35,36] The ASR was extracted from the fitted interfacial resistance normalized to the electrode area. The cell assembled without any LE exhibited a significantly large semicircle (inset, Fig. 4a). A very high ASR of ~39 800 Ω cm^2 was observed, indicating poor wetting at the LLZO/Li interface (Fig. 4b). Upon incorporating LEs, the ASR dramatically decreased (Fig. 4b). The cell utilizing the carbonate-based electrolyte showed a notable reduction to ~185 Ω cm^2, suggesting improved wetting and enhanced Li-ion transport. However, the ether-based electrolyte demonstrated an even smaller semicircle, corresponding to an exceptionally low ASR of ~32 Ω cm^2, highlighting superior interfacial contact and highly efficient ionic conduction across the LLZO/Li interface. These differences in ASR were further reflected in CCD measurements (Fig. 4c). The ether-based cell sustained a reasonably higher CCD of ~0.6 mA cm^{-2}, whereas the carbonate-based cell failed at ~0.2 mA cm^{-2}. The CCD achieved with the ether-based LE is relatively higher than values reported for many other strategies (~0.2–0.4 mA cm^2).[37–40] The lower ASR of ether-based cells minimizes interfacial defects and current localization, promoting uniform lithium deposition and effectively suppressing dendrite growth. Long term cycling tests of Li|LLZO|Li symmetric cells at 0.1 mA cm^{-2} and 60 °C further validated these findings (Fig. 4d). The cell without any LE failed to operate even for one cycle (Fig. S1b). This emphasizes the necessity of interfacial modification of LLZO. The carbonate-based symmetric cell initially exhibited reasonable cycling with an overpotential of ~61 mV; however, after ~730 h, a sudden voltage drop was observed (inset, Fig. 4d). In sharp contrast, the ether-based cell maintained exceptionally stable voltage profiles with a consistently low overpotential (~58 mV)

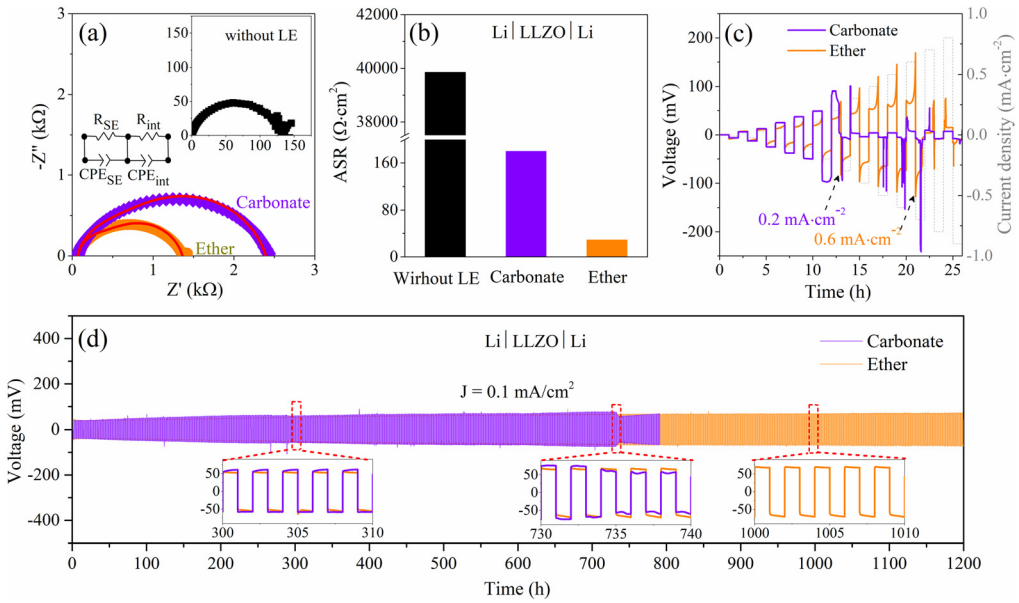

Fig. 4 Electrochemical performance comparison of Li|LLZO|Li symmetric cells: (a) Nyquist plots along with an equivalent RC circuit with and without LEs and (b) ASR values. Charge/discharge profiles (c) with increasing current density and (d) at 0.1 mA cm^{-2} for carbonate and ether-based cells, with the insets showing zoomed-out voltage profiles at selected time intervals.

over 1000 h, confirming superior long term electrochemical stability. Furthermore, even under a higher current density of 0.2 mA cm^{-2} (Fig. S2), the ether-based cell demonstrated stable cycling for 300 h with an average overpotential of ~70 mV, highlighting its excellent interfacial robustness.

To understand the origin of the observed interfacial stability, cross-sectional SEM and EIS analyses were conducted for symmetric cells assembled with and without LEs (Fig. 5). Symmetric cells without any LE showed severe interfacial gaps and poor adhesion, resulting in rapid cell degradation (Fig. S1). Both carbonate and ether-based cells exhibited excellent interfacial contact before cycling, with no major morphological differences or degradation observed after extended cycling for 300 h (Fig. 5a–d). This suggests that the application of a small amount of LE effectively improves and preserves the LLZO/Li interface. Although both carbonate and ether-based LEs initially enhanced wettability, subsequent EIS analysis revealed that the ASR increased for carbonate based cells with cycling, while ether-based systems exhibited negligible variation in impedance, maintaining superior interfacial stability during long term cycling (Fig. 5e and f). These results align with the voltage stability trends observed in Fig. 4d (Fig. S3), reinforcing that strategic interfacial engineering with optimized electrolyte formulations is essential for achieving a stable LLZO/Li interface for durable LLZO-based lithium metal batteries.

To gain deeper insight into the interfacial chemistry/stability observed in symmetric cells with carbonate and ether-based LEs, high resolution XPS analysis was conducted on pristine LLZO and LLZO surfaces after LE exposure (Fig. 6). Spectra were recorded for F 1s, N 1s, and Li 1s core levels. Due to the high surface sensitivity of XPS and the small binding energy differences between various lithium containing species, peak deconvolution is challenging and often inconsistently reported in the literature.[35,41–46] Here, we carefully analyzed the F 1s, N 1s, and Li 1s spectra using CasaXPS software, considering the underlying materials chemistry. The F 1s spectrum showed no detectable signal for pristine LLZO (Fig. 6a). Upon exposure to the carbonate-based LE, three peaks appeared at 685.4 eV, 686.9 eV, and 688.5 eV, corresponding to LiF, $Li_xPF_yO_z$, and CF_3 species, respectively (Fig. 6d).[43,45] Ether-based LE treatment resulted in a single F 1s peak at 688.8 eV, attributed to CF_3 species from the decomposition of FSI or TFSI salts (Fig. 6g). The N 1s spectrum revealed no signal for pristine or carbonate-treated LLZO (Fig. 6b and e). However, the ether-treated sample showed two peaks at 399.5 eV and 400.9 eV, corresponding to Li_3N and LiN_xO_y, indicating the formation of nitrogen rich interphases (Fig. 6h).[47,48] The Li 1s region was often omitted or briefly discussed in many previous studies due to the overlapping signals of Li_2O, LiOH, Li_2CO_3, LiF, $LiPF_6$, and $Li_xPF_yO_z$.[49] In our case, the Li 1s spectrum of pristine LLZO exhibited two peaks centered at ~54.9 and 55.5 eV, associated with Li–O (LLZO lattice) and Li_2CO_3 (Fig. 6c).[50] For carbonate-treated LLZO, peaks were observed at binding energies of ~55.1 and 56.0 eV. These were assigned to LLZO and LiF, respectively.[42,50] In the case of the ether-based system, peaks at ~55.2 and 56.2 eV were ascribed to Li_3N and LiF, respectively (Fig. 6i).[44,51] These XPS findings suggest that native Li_2CO_3 on the LLZO surface decomposes upon contact with both electrolyte types, forming chemically distinct interphases. This was further supported by Fourier transform infrared spectroscopy (FTIR) analysis (Fig. S4). Pristine LLZO exhibi-

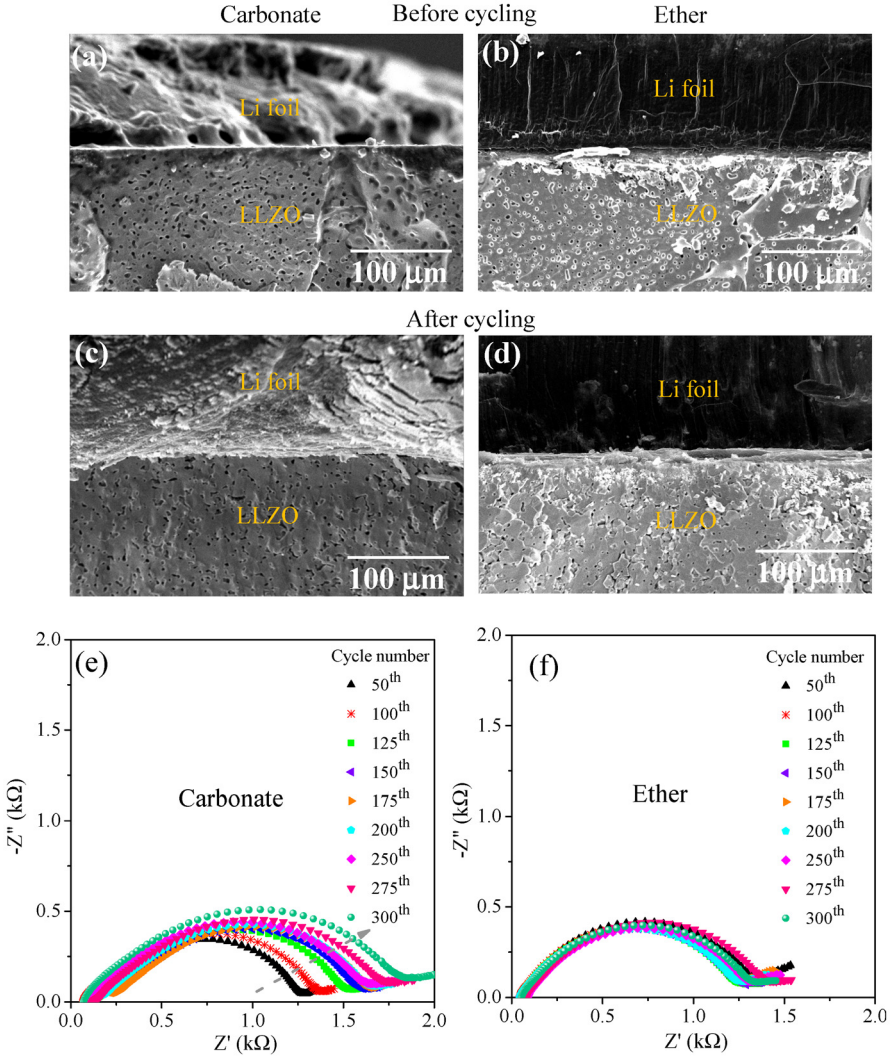

Fig. 5 (a–d) Cross-sectional SEM images and (e–f) impedance evolution profiles of Li|LLZO|Li symmetric cells utilizing carbonate and ether based LEs with cycling.

ted two characteristic absorption bands at ~1430 cm^{-1} and ~850 cm^{-1}, which match well with the carbonate groups of Li_2CO_3.[44,52] These bands disappeared after wetting with both carbonate and ether-based LEs and thermal treatment, confirming the Li_2CO_3 conversion into LiF, Li_3N, and $Li_xPF_yO_z$ depending on the electrolyte type.

To visualize the interfacial chemistry, schematic illustrations were developed (Fig. 7). In the absence of LE, a substantial interfacial gap exists between Li metal and LLZO due to the presence of native Li_2CO_3, resulting in poor contact, high ASR, and immediate cell failure (Fig. 7a). Carbonate-based LE reacts to form LiF and $Li_xPF_yO_z$ rich interphases (along with minor CF_3 species), reducing ASR and improving interface stability (Fig. 7b). An ether-based system forms highly conductive interphases dominated by Li_3N and LiF (with minor CF_3 and LiN_xO_y species), leading to enhanced wetting, much lower ASR, higher critical current density, and excellent long term cycling performance (Fig. 7c).

To assess the practical viability of the developed interfacial engineering strategy, Li|LLZO|LFP full cells were assembled using LLZO as SE, LFP as the cathode, and an ether-based LE to enhance interfacial wettability on both sides of the LLZO pellet (schematic shown in the inset of Fig. 8a). Equivalent circuit modeling of the Nyquist plot reveals a low interfacial resistance of ~36 Ω cm^2 and capacitance values in the range of 10^{-7} F, confirming efficient Li-ion transport and excellent compatibility at both the LLZO/Li and LLZO/LFP interfaces (Fig. 8a). The charge/discharge profiles at 0.1C exhibit highly stable voltage plateaus around 3.5 V, characteristic of the LFP redox couple, with minimal polarization and voltage hysteresis over 100 cycles (Fig. 8b). As shown in Fig. 8c, the full cell delivers an initial discharge capacity of ~127.4 mAh g^{-1}, gradually decreasing to ~100.3 mAh g^{-1} after 100 cycles, corresponding to a capacity retention of 78.5%. This moderate capacity fade reflects good durability for a hybrid solid-state system. Moreover, the CE remains exceptionally high

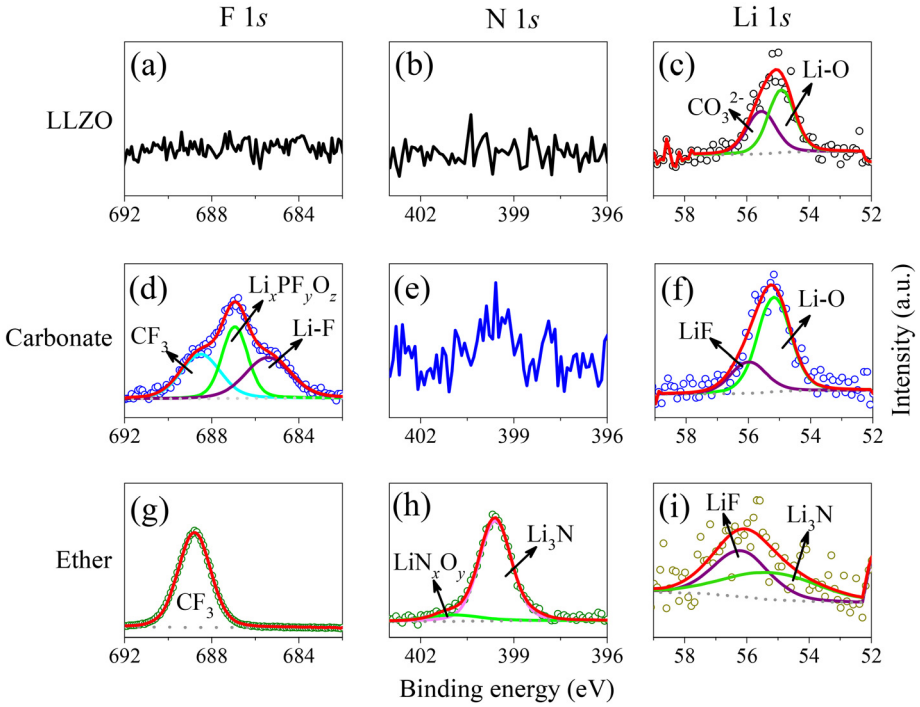

Fig. 6 XPS spectra of LLZO before and after wetting with carbonate and ether-based LEs: (a, d, g) F 1s, (b, e, h) N 1s, and (c, f, i) Li 1s.

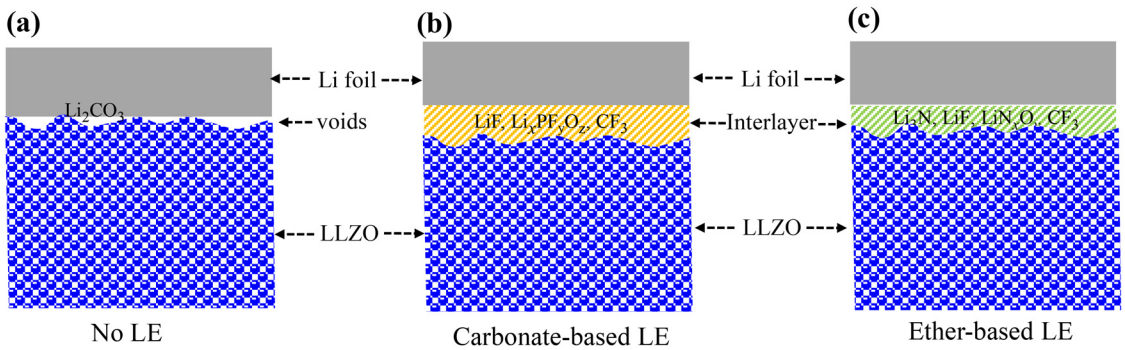

Fig. 7 Schematic of LLZO/Li interfacial structures with and without LEs: (a) poor contact without LE, (b) improved interfacial contact with carbonate-based LE, and (c) enhanced interfacial contact with ether-based LE, with each of them forming a different reaction product.

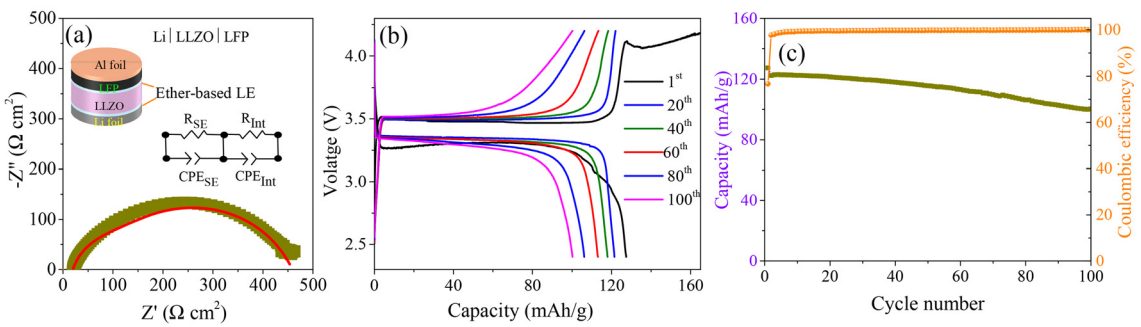

Fig. 8 Electrochemical performance of the Li|LLZO|LFP full cell with ether-based LE. (a) Nyquist plot showing low interfacial resistance, with the full cell configuration and an equivalent circuit model depicted in the insets. (b) Charge/discharge voltage profiles at a 0.1C rate for selected cycles. (c) Cycling performance of the full cell.

(~99.9%) throughout cycling, indicating minimal parasitic reactions and excellent reversibility. In contrast, the full cell utilizing a carbonate-based LE exhibited significantly poorer capacity retention and unstable cycling performance (Fig. S5). These results clearly demonstrate that the strategic use of ether-based LE enables long term cycling stability and reliable electrochemical performance in LLZO-based hybrid solid-state batteries.

4. Conclusion

The interfacial compatibility of cubic phase, highly conductive, and densely sintered LLZO was systematically investigated using minimal amounts of carbonate and ether-based LEs. Carbonate-based cells exhibited a high interfacial resistance of 185 Ω cm^2 and a low critical current density of 0.2 mA cm^{-2}, limiting their electrochemical performance. In contrast, ether-based systems significantly reduced the interfacial resistance to 32 Ω cm^2 and achieved a higher CCD of 0.6 mA cm^{-2}, attributed to the formation of a stable Li_3N/LiF rich interphase. As a result, ether-based symmetric cells showed outstanding long term stability for over 1000 h with a consistently low overpotential of 58 mV. Full cell tests further confirmed the compatibility and stability of LLZO with ether-based systems, achieving 78.5% capacity retention and 99.9% coulombic efficiency over extended cycling. These findings emphasize the potential of minimal LE usage to optimize SE/electrode interfaces, for scalable and high performance next generation battery technologies.

Author contributions

Mohammad Nasir led the methodology, experimental work, data collection, investigation, analysis, validation, and original draft writing. Jun Seo assisted in the experimental work and draft review. Seo In Jung contributed to the data collection and validation. Hee Jung Park supervised the project, and handled the conceptualization, project administration, funding, communication, and draft review.

Conflicts of interest

There are no conflicts to declare.

Data availability

The data that support the findings of this study are present in the main manuscript or its SI. The data can also be available from the corresponding author upon reasonable request.

Supplementary information is available. See DOI: **https://doi.org/10.1039/d5eb00026b**

Acknowledgements

This research was supported by the National Research Foundation (NRF) of Korea, funded by the Government of Korea (MSIT) (research project number: RS-2023-00236572). We thank the members of Prof. J. Liu's group for valuable discussions.

References

1 M. Wan, R. Gilles, J. Vacik, H. Liu, N. L. Wu, S. Passerini and D. Bresser, *Small*, 2024, **20**, 2404437.
2 M. Gao, H. Li, L. Xu, Q. Xue, X. Wang, Y. Bai and C. Wu, *J. Energy Chem.*, 2021, **59**, 666–687.
3 S. Zhang, R. Li, N. Hu, T. Deng, S. Weng, Z. Wu, D. Lu, H. Zhang, J. Zhang, X. Wang, L. Chen, L. Fan and X. Fan, *Nat. Commun.*, 2022, **13**, 1–12.
4 X. Liu, A. Mariani, H. Adenusi and S. Passerini, *Angew. Chem., Int. Ed.*, 2023, **62**, e202219318.
5 Z. Huang, Z. Xiao, R. Jin, Z. Li, C. Shu, R. Shi, X. Wang, Z. Tang, W. Tang and Y. Wu, *Energy Environ. Sci.*, 2024, **17**, 5365–5386.
6 B. Khan, M. Nasir, J.-W. Lee, H. Jung and H. J. Park, *Batteries Supercaps*, 2025, e202500227.
7 J. S. Park, M. Nasir, D. Kim, H. M. Jeong and H. J. Park, *Batteries Supercaps*, 2025, e202400741.
8 M. Nasir, J. Seo, J. S. Park, S. I. Jung, H. J. Kim and H. J. Park, *Ceramist*, 2024, **27**, 1–8.
9 S. Kim, J. S. Kim, L. Miara, Y. Wang, S. K. Jung, S. Y. Park, Z. Song, H. Kim, M. Badding, J. M. Chang, V. Roev, G. Yoon, R. Kim, J. H. Kim, K. Yoon, D. Im and K. Kang, *Nat. Commun.*, 2022, **13**, 1883.
10 S. I. Jung, M. Nasir and H. J. Park, *ACS Appl. Energy Mater.*, 2025, **8**, 9302–9310.
11 S. I. Jung, M. Nasir and H. J. Park, *J. Mater. Chem. A*, 2025, **13**, 4624–4633.
12 J. Seo, M. Nasir and H. J. Park, *ACS Appl. Energy Mater.*, 2025, **8**, 1518–1525.
13 M. Nasir, J. Seo, J. S. Park and H. J. Park, *J. Eur. Ceram. Soc.*, 2024, **44**, 4606–4611.
14 M. Nasir, J. Y. Park, P. Heo, K. H. Choi and H. J. Park, *Adv. Funct. Mater.*, 2023, **33**, 2303397.
15 C. Zhu, T. Fuchs, S. A. L. Weber, F. H. Richter, G. Glasser, F. Weber, H. J. Butt, J. Janek and R. Berger, *Nat. Commun.*, 2023, **14**, 1–14.
16 J. Gao, J. Zhu, X. Li, J. Li, X. GuO, H. Li and W. Zhou, *Adv. Funct. Mater.*, 2021, **31**, 2001918.
17 Z. Ning, G. Li, D. L. R. Melvin, Y. Chen, J. Bu, D. Spencer-Jolly, J. Liu, B. Hu, X. Gao, J. Perera, C. Gong, S. D. Pu, S. Zhang, B. Liu, G. O. Hartley, A. J. Bodey, R. I. Todd, P. S. Grant, D. E. J. Armstrong, T. J. Marrow, C. W. Monroe and P. G. Bruce, *Nature*, 2023, **618**, 287–293.
18 W. Luo, Y. Gong, Y. Zhu, K. K. Fu, J. Dai, S. D. Lacey, C. Wang, B. Liu, X. Han, Y. Mo, E. D. Wachsman and L. Hu, *J. Am. Chem. Soc.*, 2016, **138**, 12258–12262.

19 K. K. Fu, Y. Gong, B. Liu, Y. Zhu, S. Xu, Y. Yao, W. Luo, C. Wang, S. D. Lacey, J. Dai, Y. Chen, Y. Mo, E. Wachsman and L. Hu, *Sci. Adv.*, 2017, **3**, e1601659.
20 G. V. Alexander, S. Patra, S. V. S. Raj, M. K. Sugumar, M. M. Ud Din and R. Murugan, *J. Power Sources*, 2018, **396**, 764–773.
21 J. Tang, Y. Niu, Y. Zhou, S. Chen, Y. Yang, X. Huang and B. Tian, *ACS Appl. Mater. Interfaces*, 2023, **15**, 5345–5356.
22 Z. Pan, S. Cao, X. Lu, G. Zhang, Q. Shen, C. Mao, X. Dai and F. Chen, *J. Mater. Chem. A*, 2023, **11**, 20676–20685.
23 A. Sharafi, E. Kazyak, A. L. Davis, S. Yu, T. Thompson, D. J. Siegel, N. P. Dasgupta and J. Sakamoto, *Chem. Mater.*, 2017, **29**, 7961–7968.
24 R. Inada, S. Yasuda, H. Hosokawa, M. Saito, T. Tojo and Y. Sakurai, *Batteries*, 2018, **4**, 26.
25 X. Liu, Z. Xiao, H. Peng, D. Jiang, H. Xie, Y. Sun, S. Zhong, Z. Qian and R. Wang, *Chem.– Asian J.*, 2022, **17**, e202200929.
26 S. Li, J. Wang, F. Ji, M. Wang, Z. Hu, S. Huo, S. Zhang, H. Cheng and Y. Zhang, *J. Power Sources*, 2024, **592**, 233969.
27 T. Thompson, J. Wolfenstine, J. L. Allen, M. Johannes, A. Huq, I. N. David and J. Sakamoto, *J. Mater. Chem. A*, 2014, **2**, 13431–13436.
28 D. Kim, M. H. Nguyen, S. H. Chun, J. Jeon, B. K. Kim and S. Park, *Int. J. Energy Res.*, 2024, **2024**, 9050890.
29 W. Jeong, S. S. Park, J. Yun, H. R. Shin, J. Moon and J. W. Lee, *Energy Storage Mater.*, 2023, **54**, 543–552.
30 X. Zhang, C. Li, W. Liu, T. S. Oh and J. W. Fergus, *Solid State Ionics*, 2021, **369**, 115713.
31 D. Rettenwander, G. Redhammer, F. Preishuber-Pflügl, L. Cheng, L. Miara, R. Wagner, A. Welzl, E. Suard, M. M. Doeff, M. Wilkening, J. Fleig and G. Amthauer, *Chem. Mater.*, 2016, **28**, 2384–2392.
32 R. Wagner, G. J. Redhammer, D. Rettenwander, A. Senyshyn, W. Schmidt, M. Wilkening and G. Amthauer, *Chem. Mater.*, 2016, **28**, 1861–1871.
33 X. Tao, L. Yang, J. Liu, Z. Zang, P. Zeng, C. Zou, L. Yi, X. Chen, X. Liu and X. Wang, *J. Alloys Compd.*, 2023, **937**, 168380.
34 X. Huang, T. Xiu, M. E. Badding and Z. Wen, *Ceram. Int.*, 2018, **44**, 5660–5667.
35 S. A. Pervez, G. Kim, B. P. Vinayan, M. A. Cambaz, M. Kuenzel, M. Hekmatfar, M. Fichtner and S. Passerini, *Small*, 2020, **16**, 2000279.
36 M. Naguib, A. Sharafi, E. C. Self, H. M. Meyer, J. Sakamoto and J. Nanda, *ACS Appl. Mater. Interfaces*, 2019, **11**, 42042–42048.
37 Y. Li, X. Chen, A. Dolocan, Z. Cui, S. Xin, L. Xue, H. Xu, K. Park and J. B. Goodenough, *J. Am. Chem. Soc.*, 2018, **140**, 6448–6455.
38 X. He, F. Yan, M. Gao, Y. Shi, G. Ge, B. Shen and J. Zhai, *ACS Appl. Mater. Interfaces*, 2021, **13**, 42212–42219.
39 J. Wen, Y. Huang, J. Duan, Y. Wu, W. Luo, L. Zhou, C. Hu, L. Huang, X. Zheng, W. Yang, Z. Wen and Y. Huang, *ACS Nano*, 2019, **13**, 14549–14556.
40 T. Panneerselvam, R. Murugan and O. V. Sreejith, *ACS Appl. Energy Mater.*, 2024, **7**, 1700–1709.
41 J. Liu, X. Gao, G. O. Hartley, G. J. Rees, C. Gong, F. H. Richter, J. Janek, Y. Xia, A. W. Robertson, L. R. Johnson and P. G. Bruce, *Joule*, 2020, **4**, 101–108.
42 J. Leng, H. Wang, Y. Li, Z. Xiao, S. Wang, Z. Zhang and Z. Tang, *Appl. Surf. Sci.*, 2022, **575**, 151638.
43 P. Jiang, J. Cao, B. Wei, G. Qian, S. Wang, Y. Shi, G. Du, X. Lu, C. Ouyang, F. Cao and X. Lu, *Energy Storage Mater.*, 2022, **48**, 145–154.
44 N. Chen, B. Gui, B. Yang, C. Deng, Y. Liang, F. Zhang, B. Li, W. Sun, F. Wu and R. Chen, *Small*, 2024, **20**, 2305576.
45 Y. Guo, S. Pan, X. Yi, S. Chi, X. Yin, C. Geng, Q. Yin, Q. Y. Zhan, Z. Zhao, F. M. Jin, H. Fang, Y. B. He, F. Kang, S. Wu and Q. H. Yang, *Adv. Mater.*, 2024, **36**, 2308493.
46 S. Sarkar, B. Chen, C. Zhou, S. N. Shirazi, F. Langer, J. Schwenzel and V. Thangadurai, *Adv. Energy Mater.*, 2023, **13**, 2203897.
47 Y. Liang, W. Wu, D. Li, H. Wu, C. Gao, Z. Chen, L. Ci and J. Zhang, *Adv. Energy Mater.*, 2022, **12**, 2202493.
48 B. Liu, Y. Zhang, Z. Wang, C. Ai, S. Liu, P. Liu, Y. Zhong, S. Lin, S. Deng, Q. Liu, G. Pan, X. Wang, X. Xia and J. Tu, *Adv. Mater.*, 2020, **32**, 2003657.
49 A. M. Tripathi, W. N. Su and B. J. Hwang, *Chem. Soc. Rev.*, 2018, **47**, 736–851.
50 W. Xia, B. Xu, H. Duan, Y. Guo, H. Kang, H. Li and H. Liu, *ACS Appl. Mater. Interfaces*, 2016, **8**, 5335–5342.
51 Y. X. Wang, S. K. Hong, H. P. Hsu and C. W. Lan, *Adv. Mater. Technol.*, 2024, **9**, 2400116.
52 V. Janakiraman, M. Savio, A. N. Alodhayb, M. Muthuramamoorthy, M. A. Dhanalakshmi, M. Vimalan, M. Durai and K. Ganesh Kumar, *J. Mater. Sci.: Mater. Electron.*, 2025, **36**, 1–16.